J. Fluid Mech. (2000), *vol.* 418, *pp.* 167–188. Printed in the United Kingdom

Experimental evidence for a new instability of a vertical columnar vortex pair in a strongly stratified fluid

By PAUL BILLANT[1,2]† AND JEAN-MARC CHOMAZ[1]

[1]LadHyX, CNRS, École Polytechnique, F–91128 Palaiseau Cedex, France
[2]Météo–France CNRM Toulouse, 42 avenue Coriolis, F–31057 Toulouse, France

(Received 1 November 1999)

This paper shows that a long vertical columnar vortex pair created by a double flap apparatus in a strongly stratified fluid is subjected to an instability distinct from the Crow and short-wavelength instabilities known to occur in homogeneous fluid. This new instability, which we name zigzag instability, is antisymmetric with respect to the plane separating the vortices. It is characterized by a vertically modulated twisting and bending of the whole vortex pair with almost no change of the dipole's cross-sectional structure. No saturation is observed and, ultimately, the vortex pair is sliced into thin horizontal layers of independent pancake dipoles. For the largest Brunt–Väisälä frequency $N = 1.75\,\mathrm{rad\,s^{-1}}$ that may be achieved in the experiments, the zigzag instability is observed only in the range of Froude numbers: $0.13 < F_{h0} < 0.21$ ($F_{h0} = U_0/NR$, where U_0 and R are the initial dipole travelling velocity and radius). When $F_{h0} > 0.21$, the elliptic instability develops resulting in three-dimensional motions which eventually collapse into a relaminarized vortex pair. Irregular zigzags are then also observed to grow. The threshold for the inhibition of the elliptic instability $F_{h0} = 0.2 \pm 0.01$ is independent of N and in good agreement with the theoretical study of Miyazaki & Fukumoto (1992). Complete stabilization for $F_{h0} < 0.13$ is probably due to viscous effects since the associated Reynolds number is low, $Re_0 < 260$. In geophysical flows characterized by low Froude numbers and large Reynolds numbers, we conjecture that this viscous stabilization will occur at much lower Froude number.

It is tentatively argued that this new type of instability may explain the layering widely observed in stratified turbulent flows.

1. Introduction

Fluid motions in the atmosphere and oceans are often strongly affected by stable density stratification. In these flows, large vertical motions are inhibited by the buoyancy force, leaving only two possible modes of motion: internal gravity waves and vortices with vertical axis (Riley, Metcalfe & Weissman 1981). Laboratory experiments (Lin & Pao 1979; Hopfinger 1987; Chomaz *et al.* 1993; Fincham, Maxworthy & Spedding 1996; Spedding, Browand & Fincham 1996; Spedding 1997; Bonnier, Eiff & Bonneton 2000), numerical simulations (Riley *et al.* 1981; Herring & Métais 1989; Métais & Herring 1989; Kimura & Herring 1996) and oceanic measurements (Gregg 1987) have revealed that these vortices never have a large vertical extent, but are

† Present address: Météo–France CNRM Toulouse, 42 avenue Coriolis, F–31057 Toulouse, France.

rather thin like 'pancakes'. It is now well known that this layered flow structure enhances energy dissipation through the associated strong vertical shear (Herring & Métais 1989; Métais & Herring 1989; Fincham *et al.* 1996). This feature has been invoked as the reason why stratified turbulence departs profoundly from two-dimensional turbulence although the motion is mostly horizontal (Herring & Métais 1989; Métais *et al.* 1996). However, despite its importance in understanding turbulence in geophysical flows, the reason why the vortices acquire such a flat 'pancake' shape remains unclear: is such layering due to the initial collapse of three-dimensional motions under the gravitational restoring force or is it an intrinsic behaviour of vertical vortices in the presence of stable stratification?

Some results of the numerical simulations of two-dimensionally forced stratified turbulence by Herring & Métais (1989) suggest that the layering may arise as a result of an instability. The initial conditions of these numerical experiments consisted of a forced turbulent flow vertically uniform, i.e. purely two-dimensional, upon which a three-dimensional perturbation was added. This disturbance grew exponentially and resulted in the formation of decoupled layers. However, the physical mechanism of this instability remains unexplained. The vertical cylinder wakes experiments of Fincham *et al.* (1996) also show that layers can emerge from a vertically coherent flow.

In an attempt to further elucidate the mechanism by which decoupled layers arise, we investigate the dynamics of a simple prototype flow initially uniform along the vertical: a pair of long counter-rotating vertical columnar vortices in a strongly stratified fluid. The vortex pair is created by means of computer-controlled 'flaps' made of two rotating vertical plates.

In a homogeneous fluid, such a vortex pair has been studied in detail because of its aeronautical interest. It is subject to two three-dimensional instabilities: a long-wavelength Crow instability characterized by symmetric sinusoidal deformations of the two vortices (Crow 1970) and a recently identified short-wavelength antisymmetric instability related to the elliptic instability of the vortex core (Thomas & Auerbach 1994; Leweke & Williamson 1998). The terms symmetric and antisymmetric refer to the symmetry of the perturbation with respect to the middle plane between the two vortices.

The presence of stratification radically modifies this picture. When buoyancy effects are dominant, the Crow and elliptic instabilities are inhibited and we show in the present study that a third type of instability spontaneously slices the columnar vortex pair into thin horizontal layers of pancake-like dipoles. This instability, which we name zigzag instability, occurs only when the fluid is strongly stratified and clearly differs from the Crow and elliptic three-dimensional instabilities. This paper is devoted to a detailed characterization of this new instability.

The present experimental study has initiated two companion papers (Billant & Chomaz 2000*a*, *b*) aimed at further understanding the zigzag instability. These two studies both analyse the stability of a columnar vortex pair in a stratified fluid but using different means: either asymptotical for small Froude number (Billant & Chomaz 2000*a*) or numerical (Billant & Chomaz 2000*b*). For the moment, it is sufficient to say that these two investigations confirm the existence of the zigzag instability and, together with the present experimental study, give a complete and consistent description of the zigzag instability. By the end of the present paper, the purposes of these companion studies will be clearer. A discussion on their motivations is therefore naturally postponed to the concluding section.

The paper is organized as follows. The experimental set-up and procedure are presented in § 2. Velocity fields of the basic vortex pair are shown in § 3. Stratification

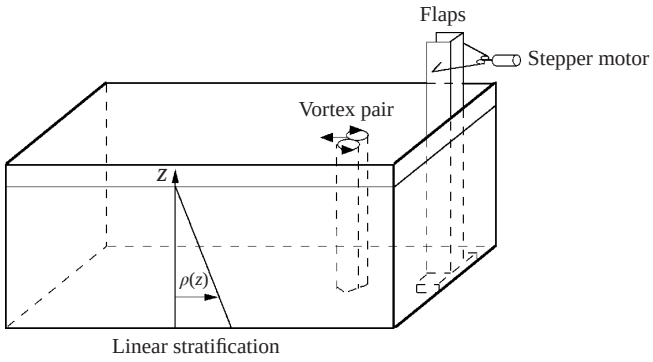

FIGURE 1. Sketch of experimental set-up.

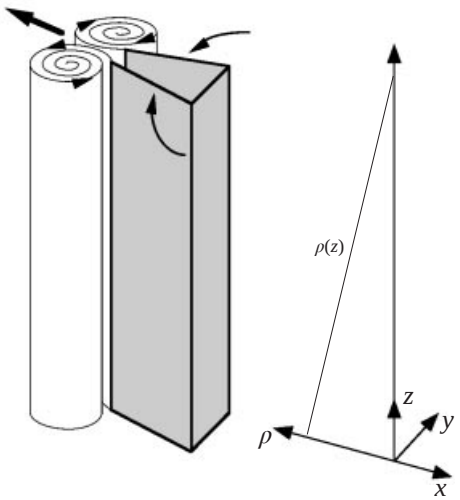

FIGURE 2. Sketch of the 'flap' apparatus used to produce a columnar vertical vortex pair in a stratified fluid.

effects on the elliptic instability are described in § 4.1. In § 4.2, the threshold at which the elliptic instability is suppressed is compared to the theoretical study of Miyazaki & Fukumoto (1992). In § 4.3, the zigzag instability is characterized by means of flow visualizations. The pancake structure which is produced is briefly described in § 4.4. Wavelength and growth rate measurements are presented in § 4.5 and § 4.6, respectively.

2. Experimental set-up and procedure

The experiments are performed in a 100 cm wide, 200 cm long and 70 cm deep glass tank (figure 1). The tank is filled with a linearly stratified salt solution with a 65 cm working depth. The stratification is established by the well-known two tank method by means of two computer-controlled volumetric pumps.

A 60 cm columnar vertical vortex pair is created by suddenly closing two long vertical 'flaps', as one would close an open book (figure 2). The flaps are similar to those used by Leweke & Williamson (1998). They consist of two aluminium plates 10.1 cm wide and 100 cm long with one vertical edge sharpened and the other hinged to a vertical base 6.3 cm wide (figure 2). The flap motion is driven through a system

of gears by a computer-controlled stepper motor. When the two vertical plates, initially parallel, are moved towards each other, each through the same closing angle α, the shear layers generated at the moving edges roll up into two starting vortices that propagate away by mutual induction (figure 2). The rotation rate of the flaps decreases linearly to zero during the course of the motion. Two small stopping vortices are created at the end of the motion. Preliminary experiments with closing angle α smaller than 12° have shown that these stopping vortices are then advected by the starting vortices and begin orbiting around them leading to a spurious instability. Such behaviour has never been observed when the closing angle α is larger than 12° because the stopping vortices are then trapped inside the cavity formed by the nearly closed flaps preventing them from disturbing the starting vortices. However, the closing angle α should not be too large in order to avoid strong expulsion of the inner fluid at the end of the flap motion. Thus, a 14° angle has been found to be a good compromise between these two requirements. All the experiments reported here use this value of α so that only the closing time T is varied. In order to minimize end effects, the flaps are bounded at the bottom with a flat cover fixed on a 5 cm high pedestal. The flap apparatus is set up slightly off-centred against one of the 100 cm wide tank walls. It is mounted on a vertical sliding carriage driven by a motor so that it can be slowly immerged and taken out of the water.

The flow is visualized by UV induced fluorescence. Fluorescent dye is painted on the inner side of the vertical plates when the flap apparatus is out of the water. Once the dye is dry, the apparatus is lowered extremely slowly into the tank. Upon closing the flaps, the dissolved dye is engulfed into the vortices, allowing the flow to be visualized. With one dye painting, it is generally possible to make three experiments. The light source consists of three 100 W UV lamps placed underneath the tank. Quiescent flow conditions are reached by waiting at least 30 min between each experiment. Between each experiment, the UV lamps are switched off in order to avoid heating of the water. Frontal and side view images are simultaneously recorded with black and white 740×480 pixels CCD cameras and video recorders. The side camera is mounted on a traversing mechanism which allows the vortex pair to be followed over most of its displacement. The speed of the traversing device is constant and adjusted before each experiment to the expected translating velocity of the vortex pair. The instability wavelength is measured from the frontal images, where deformations are best seen. However, a difficulty arises because the apparent size of the vortex pair increases on these images as it is coming toward the camera. In order to circumvent this difficulty and obtain accurate measurements, a reference lengthscale is provided by two parallel laser light rays going horizontally through the tank from the side. This laser source is also mounted on the traversing device so that the light rays are always maintained in the vicinity of the vortex pair. Various procedures such as wavelength and propagating speed measurements are carried out on the images by making use of the public domain NIH image processing software (developed at the US National Institute of Health and available on the Internet at http://rsb.info.nih.gov/nih-image/) on a Macintosh. For the purpose of showing colour images in the present paper, one experiment has been filmed with two colour cameras, one viewing from the front, the other obliquely from the side (and not at 90° as for the black and white camera used for the measurements). The latter camera travels with the vortex pair.

The procedure to measure the Brunt–Väisälä frequency N is somewhat original: a small cylinder located near the centre of the tank is oscillated vertically at a given frequency f. The angle ϕ relative to the horizontal of the St. Andrew's cross pattern

made by internal wave rays is measured using shadowgraph visualizations for several oscillating frequencies f. Then, the Brunt–Väisälä frequency is deduced from the dispersion relation $2\pi f = N \sin\phi$ by a regression fit between f and the corresponding measured angles ϕ. This procedure has been tested against density measurements made by withdrawing small samples of fluid at different heights. The values of N determined by the two methods typically differ by less than 2%. The constancy of N over the depth is also checked by verifying that ϕ does not vary with height. Such a measurement is made at the beginning of a set of experiments and also at the end in order to check that the linear stratification has not been altered.

For each experiment, the propagating velocity U of the dipole is measured from the side views by tracking the displacement of one edge of the vortex pair every second over approximately a 50 s time period. The measurements are started shortly after the end of the flap motion.

In some experiments, the correlation image velocimetry (CIV) technique of Fincham & Spedding (1997) is used to determine quantitatively the initial horizontal velocity field. The flow is seeded with small polystyrene beads of mono-dispersed density $1.04\,\mathrm{g\,cm^{-3}}$ which floated in a thin horizontal layer where they are neutrally buoyant. This layer is lighted uniformly from above. Pairs of images are acquired sequentially with a time interval of $\delta t = 0.067\,\mathrm{s}$ by a 768×484 pixels TM-9701 Pulnix digital camera. The recorded area under the camera is $10.6 \times 14.8\,\mathrm{cm^2}$. As explained by Fincham & Spedding (1997), this CIV technique is based on the calculation in physical space of the cross-correlation between the two successive frames. The first image is divided into small rectangular boxes and the mean displacement of a given box is determined from the cross-correlation peak location in the second image. The velocity field is next obtained on a regular Cartesian grid by accurate spline interpolation. Spatial derivatives are computed analytically from the coefficients of the spline functions.

We define two non-dimensional parameters: the horizontal Froude number which measures the competition between buoyancy and inertial forces

$$F_{h0} = \frac{U_0}{NR}, \tag{2.1}$$

where U_0 and R are the initial propagating speed and radius of the dipole and the Reynolds number

$$Re_0 = \frac{U_0 R}{\nu}, \tag{2.2}$$

where ν is the mean kinematic viscosity, i.e. the viscosity of the salt solution at the middle of the tank. Since the dipole radius R is mainly determined by the size of the flap apparatus, the two control parameters which are varied are the dipole translation speed U_0 and the Brunt–Väisälä frequency N. Therefore, for a given stratification, Re_0 and F_{h0} are related by $Re_0 = F_{h0} N R^2/\nu$ so that the Froude and Reynolds numbers vary together when U_0 is varied.

3. Basic state

In this section, we describe quantitatively the two-dimensional vortex pair which is produced by the flap mechanism.

An example of the displacement of the dipole as measured from the side views is shown in figure 3. This curve can be fitted by an exponentially decaying function

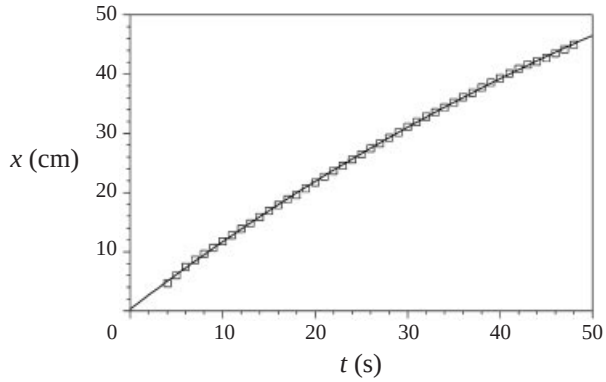

FIGURE 3. Displacement of the dipole as a function of time for $F_{h0} = 0.19$ and $Re_0 = 365$. The solid line is an exponential fit.

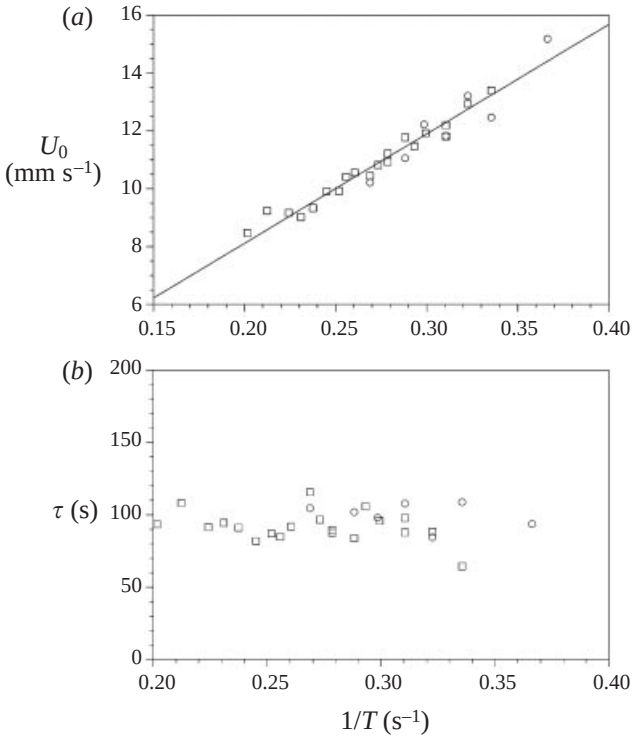

FIGURE 4. (*a*) Initial translation speed U_0 and (*b*) viscous decay time τ of the dipole as a function of the inverse of the closing time T. □, $N = 1.75\,\mathrm{rad\,s^{-1}}$; ○, $N = 1.70\,\mathrm{rad\,s^{-1}}$.

from which the travelling velocity at every time can be obtained in the form

$$U = U_0\,\mathrm{e}^{-t/\tau}, \tag{3.1}$$

where τ is the decay time. These measurements have been carried out for all the closing times T investigated (the closing angle, $\alpha = 14°$, being constant). As shown in figure 4(*a*), the initial propagation speed of the vortex pair U_0 is inversely proportional to the closing time T: the faster the flaps are closed, the larger U_0. In contrast, figure 4(*b*) shows that the decay time τ is approximately constant $\tau \approx 90\,\mathrm{s}$.

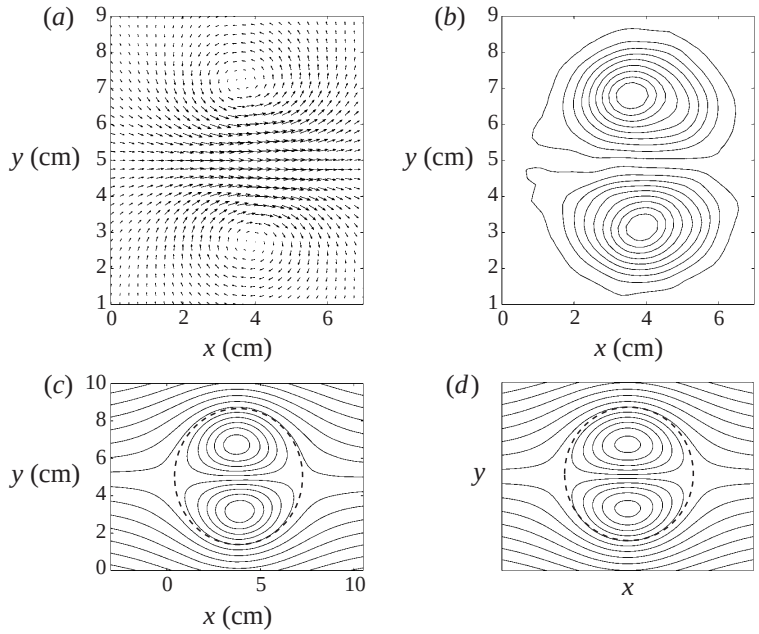

FIGURE 5. Experimental (*a*) velocity fields, (*b*) iso-vorticity lines (interval $0.4\,\mathrm{s}^{-1}$) and (*c*) streamlines in the frame of reference translating with the dipole at speed $7.9\,\mathrm{mm\,s}^{-1}$ (interval $0.52\,\mathrm{cm}^2\,\mathrm{s}^{-1}$). (*d*) Theoretical streamlines of the Lamb–Chaplygin dipole. In (*c*) and (*d*), the dashed circle indicates the boundary between open and closed streamlines.

Figures 5(*a*) and 5(*b*) show typical horizontal velocity and vertical vorticity fields measured on a 74×50 grid shortly after the end of the flap motion. As seen in figure 5(*b*), the dipole is approximately circular with a radius $R = 3.6\,\mathrm{cm}$. In the range of parameters investigated, this radius is approximately constant regardless of the closing time T. The streamfunction ψ' in the laboratory frame is computed from the vorticity field ω by solving the Poisson equation $\Delta\psi' = \omega$ by means of a numerical fast Fourier transform. In order to avoid spurious effects resulting from the periodic boundary conditions, the domain of integration is enlarged five times by setting $\omega = 0$ in the outer potential region. The streamfunction ψ in a frame of reference translating with the dipole (figure 5*c*) is calculated by applying the transformation $\psi = \psi' - u_x y + u_y x$ where u_x and u_y are the two components of the translation velocity. For comparison, figure 5(*d*) shows the streamfunction of the Lamb–Chaplygin dipole (Batchelor 1967; Meleshko & van Heijst 1994) given by

$$\psi(r,\theta) = -\frac{2UR}{\mu_1 J_0(\mu_1)} J_1\left(\mu_1 \frac{r}{R}\right)\sin\theta \quad (r \leqslant R), \tag{3.2}$$

$$\psi(r,\theta) = -Ur\left(1 - \frac{R^2}{r^2}\right)\sin\theta \quad (r > R), \tag{3.3}$$

where (r,θ) are cylindrical coordinates in the horizontal plane, J_0 and J_1 are the Bessel functions of zero and first order and $\mu_1 = 3.8317$ is the first zero of J_1. The Lamb–Chaplygin dipole is an exact solution of the Euler equations characterized by a structure function $\omega = f(\psi)$. In the rotational region $r < R$, the structure function is linear, $\omega = (\mu_1/R)^2\psi$, whereas in the potential region, $r > R$, $\omega = 0$. As seen in figures 5(*c*) and 5(*d*), the measured dipole closely resembles the Lamb–Chaplygin dipole.

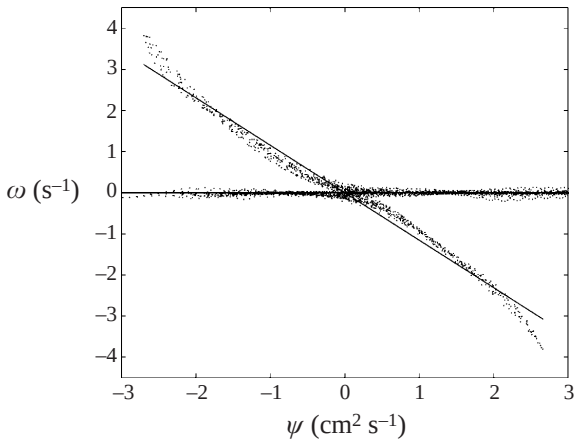

FIGURE 6. Scatter plot of the vorticity ω as a function of the streamfunction ψ in the frame of reference translating with the dipole. The solid line is a linear fit to the points with non-zero vorticity.

The values of the vorticity ω and streamfunction ψ at each point of the measurement grid are represented in a scatter plot in figure 6. The points collapse on a single curve with two branches, one of which is on the ψ axis and corresponds to the potential flow outside the dipole while the other is associated to the rotational flow inside the dipole. This behaviour indicates that the basic flow is, as expected, almost a stationary state of the two-dimensional Euler equations. Although the curve $\omega = f(\psi)$ is slightly nonlinear with a sinh-like profile as often observed (Nguyen Duc & Sommeria 1988; Flor & Van Heijst 1994), it can be reasonably well fitted to a linear function $\omega = k^2\psi$ as shown on figure 6. A least-square linear fit with the points having a non-zero vorticity gives the slope $k^2 = 1.15$ which is in good agreement with the value $k^2 = (\mu_1/R)^2 = 1.13$ for a Lamb–Chaplygin dipole with the radius $R = 3.6\,\mathrm{cm}$ measured on the contour plot (figures 5*b* and 5*c*) or from flow visualizations.

4. Results

4.1. *Stratification effects on the elliptic instability*

The effect of a weak stratification ($N = 0.88\,\mathrm{rad\,s^{-1}}$) on the Crow and elliptic instabilities has been investigated by Williamson & Chomaz (1997) using the present apparatus. Their study revealed that, for moderate travelling velocity U_0 of the vortex pair (i.e. Froude number of order unity), the Crow instability was inhibited by the stratification. Only the elliptic instability was present but, under the gravitational restoring force, the resulting three-dimensional motions rapidly collapsed into a relaminarized vortex pair. Surprisingly, large irregular vertical deformations of the relaminarized vortices were subsequently observed. Their effects was to decorrelate the flow into independent horizontal layers of pancake vortices.

We have observed the same scenario for higher stratification $N = 1.26\,\mathrm{rad\,s^{-1}}$. Since Re_0 and F_{h0} are related by $Re_0 = F_{h0}NR^2/\nu$, the effect of increasing the Brunt–Väisälä frequency is to achieve, for the same Froude number, a higher Reynolds number. As in Williamson & Chomaz (1997), only the elliptic instability develops for moderate Froude number while the Crow instability is completely inhibited as demonstrated by the absence of large-scale symmetric deformations of the vortex pair in figure 7(*a*).

This figure shows clearly that this instability is antisymmetric with respect to the

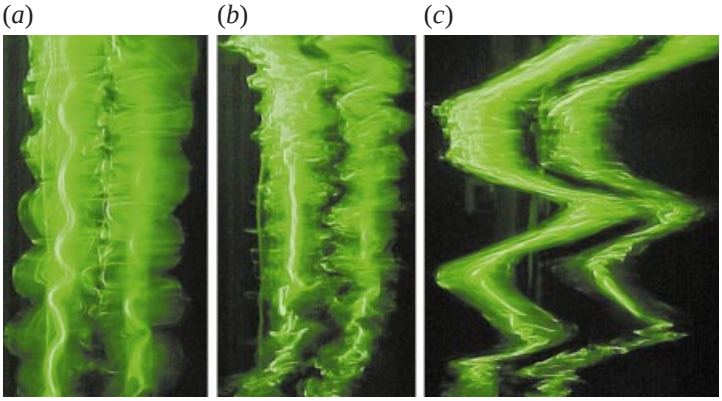

FIGURE 7. Flow visualizations of the development of the elliptic instability at (*a*) $t = 20\,\mathrm{s}$ and (*b*) $t = 35\,\mathrm{s}$ after the end of the flap motion. (*c*) Irregular zigzags ($t = 110\,\mathrm{s}$) observed after the gravitational collapse of the elliptic instability. The scales are not the same for each picture. $F_{h0} = 0.27$ and $Re_0 = 423$.

middle plane separating the two vortices as first shown by Leweke & Williamson (1998) (the core of the right-hand vortex is less visible because of a difference in lighting). Furthermore, the waviness of the inner vortex core and those of the vortex core periphery are in antiphase as described by Thomas & Auerbach (1994) and Leweke & Williamson (1998). This feature clearly identifies the first elliptic instability mode (Tsai & Widnall 1976; Waleffe 1990). These deformations quickly lead to important three-dimensional motions (figure 7*b*) which subsequently collapse under the stable stratification. Later, the collapsed vortex pair is distorted into irregular antisymmetric zigzags (figure 7*c*).

For this particular density gradient $N = 1.26\,\mathrm{rad\,s^{-1}}$, the evolution described above prevails for $F_{h0} > 0.21$ corresponding to $Re_0 > 298$. Below this threshold, the vortex pair is found to be stable and to remain vertically straight; neither the elliptic instability nor zigzag deformations develop (however, very large deformations, growing slowly, are occasionally observed probably because of residual motions in the tank).

Further increasing the stratification to $N = 1.70\,\mathrm{rad\,s^{-1}}$ and $N = 1.75\,\mathrm{rad\,s^{-1}}$, we found similar critical Froude numbers, $F_{h0} = 0.20$ and $F_{h0} = 0.21$, respectively, (corresponding to $Re_0 = 387$ and $Re_0 = 402$, respectively) below which the elliptic instability is inhibited. Strikingly, for these larger values of N, the vortex pair is not stable below this critical Froude number. As seen in figure 8, sinusoidal antisymmetric deformations, which will be shown to be very distinct from those characterizing the elliptic instability, grow without bound on the vortex pair (figure 8 will be described in more detail in § 4.3). Such behaviour demonstrates the existence of a third type of instability, which we name 'zigzag' instability. When the Froude number is further decreased below $F_{h0} < 0.13$ corresponding to $Re_0 < 254$, the vortex pair recovers its stability. Sections 4.3, 4.4 and 4.5 will focus on the new instability while § 4.2 further addresses the inhibition of the elliptic instability.

The Brunt–Väisälä frequency could not be increased above $N = 1.75\,\mathrm{rad\,s^{-1}}$ owing to the present experimental conditions. Indeed, using salt as the stratifying agent, the maximum relative difference of density is $\Delta\bar{\rho}/\bar{\rho} \approx 0.2$ with fresh water at the top of the tank and saturated brine at the bottom. In addition, there is a minimal water depth of 65 cm which is necessary to minimize the influence of end boundaries and confinement effects in the vertical direction. However, if only the threshold of inhibition of the elliptic instability is to be determined, these effects are not critical

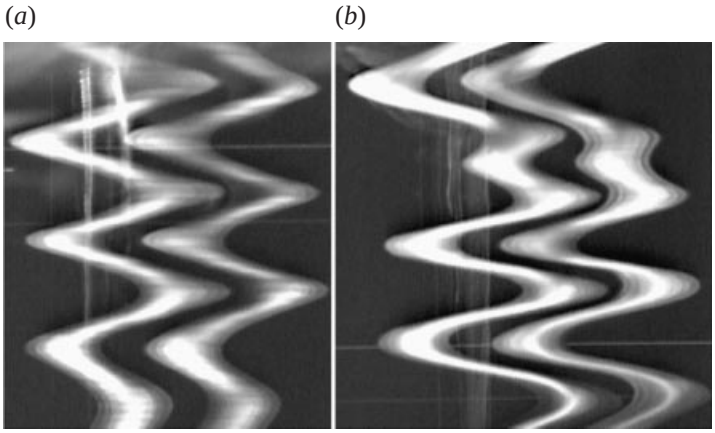

FIGURE 8. Visualizations of the zigzag instability in two different experiments in the absence of forcing for the same parameters $F_{h0} = 0.19$, $Re_0 = 365$ at $t = 121$ s after stopping the flap motion. In (*a*) a regular zigzag pattern is observed while a defect can be seen in (*b*).

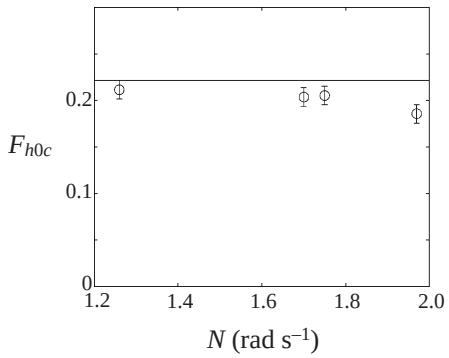

FIGURE 9. Froude number F_{h0c} of disappearance of the elliptic instability as a function of the Brunt–Väisälä frequency N. The solid line indicates the threshold deduced from the theoretical criterion of Miyazaki & Fukumoto (1992).

and the Brunt–Väisälä frequency may be increased to $N = 1.97\,\mathrm{rad\,s^{-1}}$ by reducing the water depth to 45 cm. In that case, we found that the elliptic instability is inhibited below $F_{h0} = 0.19$, i.e. very close to the critical Froude number F_{h0} obtained for lower Brunt–Väisälä frequencies.

4.2. *Froude number of inhibition of the elliptic instability by the stratification*

The critical Froude number of inhibition of the elliptic instability is $F_{h0c} = 0.2 \pm 0.01$ independently of the Brunt–Väisälä frequency N investigated (figure 9). In contrast, the corresponding Reynolds number varies between $Re_0 = 346$ and $Re_0 = 474$. This indicates that the inhibition of the elliptic instability is controlled by buoyancy effects and not by viscous effects. This value can be accounted for from the study of Miyazaki & Fukumoto (1992). They have shown theoretically that the elliptic instability is suppressed by the stratification when

$$N > (\gamma^2 - \epsilon^2)^{1/2}, \tag{4.1}$$

where 2γ is the vorticity and ϵ the strain rate of an infinite elliptical vortex given by the streamfunction

$$\psi_0 = \tfrac{1}{2}[(\gamma - \epsilon)x^2 + (\gamma + \epsilon)y^2]. \tag{4.2}$$

In the limiting case of weak strain $\epsilon/\gamma \to 0$, Miyazaki & Fukumoto (1992) have provided a clear understanding for this threshold based on the physical mechanism of the elliptic instability in homogeneous fluid (Waleffe 1990). The essence of the elliptic instability is a resonant interaction between the strain and inertial waves. In the case of the vortex (4.2) with uniform vorticity 2γ and without stratification, these inertial waves have a frequency ω in the range $0 < |\omega| < 2\gamma$ in the frame of reference rotating with angular velocity γ. The unstable resonance with the elliptic deformation (that rotates at the angular velocity γ in the rotating frame) occurs for inertial waves with the same frequency $\omega = \gamma$. This mechanism can be directly extended to inertio-gravity waves for a vertical vortex in a stratified fluid. The only difference is that the permissible range of frequency is now $N \leqslant \omega \leqslant 2\gamma$ (when $N < 2\gamma$). Therefore, as soon as $N > \gamma$, inertio-gravity waves with frequency $\omega = \gamma$ no longer exist and the elliptic instability cannot occur. When ϵ/γ is finite, the resonance occurs in a finite frequency band around γ, the resonance condition being given by (4.1).

This criterion can be applied to predict the critical Froude number of inhibition of the elliptic instability of the vortex pair. Even if the vortices of the dipole are of finite size and have a non-uniform vorticity, we postulate that the condition (4.1) for an infinite uniform vortex remains valid. The Lamb–Chaplygin dipole model is used in order to relate the local strain rate ϵ and vorticity γ at the vortex centres to the translating velocity U and radius R of the dipole. To this end, we expand the Lamb–Chaplygin streamfunction (3.2) near one vortex centre ($r_c = \mu_m/\mu_1,\ \theta_c = \pi/2$) of the pair ($\mu_m = 1.8412$ is the value at which the Bessel function J_1 is maximum in the interval $[0, \mu_1]$)

$$\psi = \tfrac{1}{2}\left[(\gamma - \epsilon)x^2 + (\gamma + \epsilon)\left(y - \frac{\mu_m}{\mu_1}\right)^2\right] + O\left(x^3, \left(y - \frac{\mu_m}{\mu_1}\right)^3, \ldots\right), \tag{4.3}$$

which yields

$$\gamma = \frac{\omega_z(r_c, \theta_c)}{2} = \mu_1 \frac{J_1(\mu_m)U}{J_0(\mu_1)R} = -5.06\frac{U}{R}, \tag{4.4}$$

$$\epsilon = \mu_1 \frac{J_1(\mu_m)U}{J_0(\mu_1)R}\left(\frac{2}{\mu_m^2} - 1\right) = 2.28\frac{U}{R}. \tag{4.5}$$

Thus, the criterion $N > (\gamma^2 - \epsilon^2)^{1/2}$ for the inhibition of the elliptic instability becomes, in terms of the horizontal Froude number, $F_{h0} < 0.22$. As seen in figure 9, the experimental critical Froude number values are close to this theoretical threshold (indicated by a solid line) despite the fact that it is based on a crude extrapolation of the Miyazaki & Fukumoto (1992) criterion.

4.3. *Observations of the zigzag instability*

The time-sequence in figure 10 shows the growth of the zigzag instability filmed simultaneously from the front, the vortex pair coming toward the camera, and obliquely from the side, the camera moving with the vortex pair. Only the upper portion of the vortex pair is shown (approximately 70% of the entire length). At the bottom, the vortex pair is less marked by dye, and deformations are affected by the presence of the bottom boundary. At the top, some dye has been dispersed away after the flaps were lowered into the tank. This dye is, however, easily distinguished from the

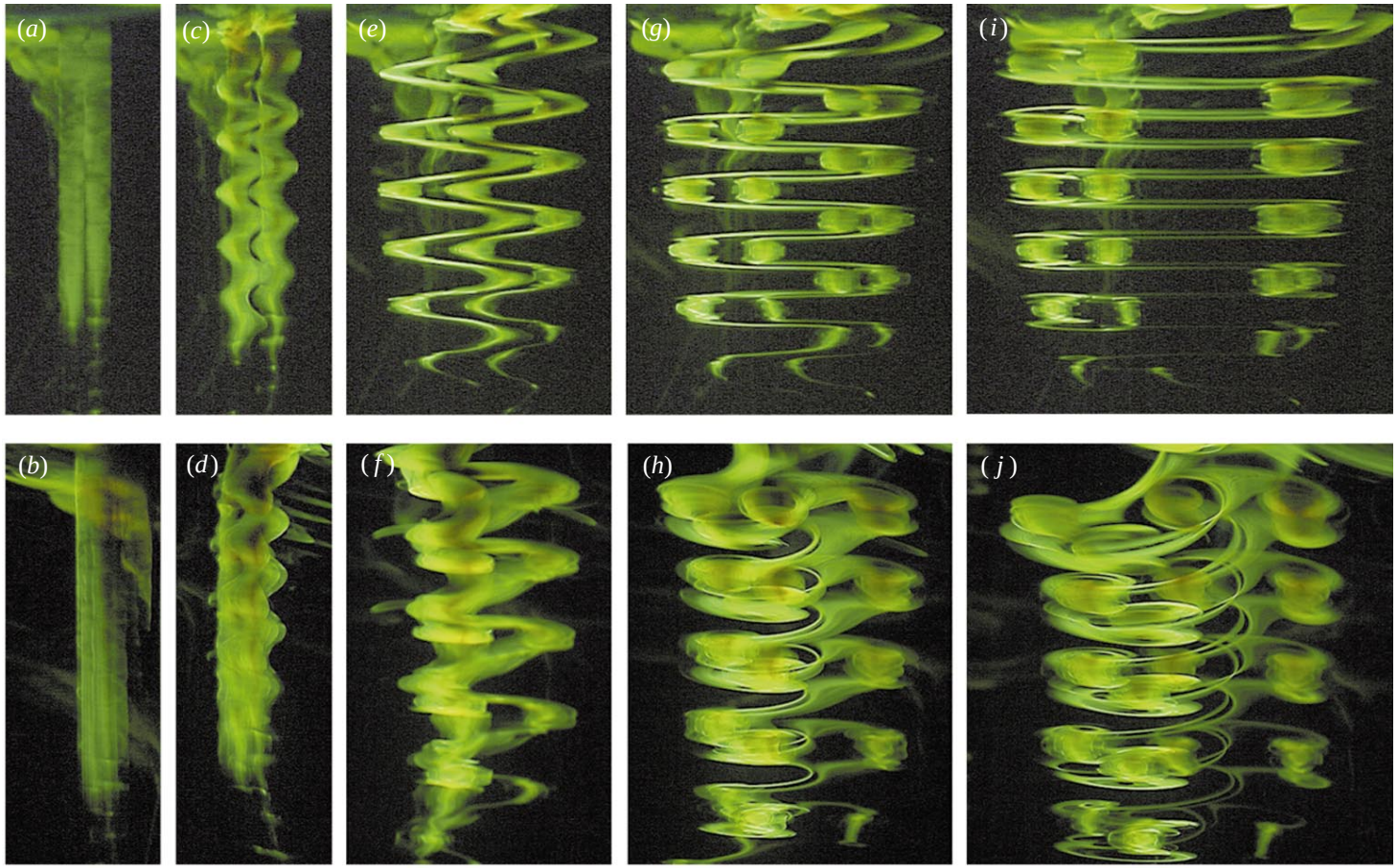

FIGURE 10. A sequence of frontal (*a*), (*c*), (*e*), (*g*), (*i*) and side (*b*), (*d*), (*d*), (*h*), (*j*) views showing the growth of the zigzag instability for $F_{h0} = 0.19$ and $Re_0 = 365$. The pictures have been taken at 7 s (*a*), (*b*); 36 s (*c*), (*d*); 75 s (*e*); 109 s (*d*); 121 s (*g*), (*h*); 176 s (*i*), (*j*) after stopping the flap motion. In the side views, the vortex pair is initially propagating leftward. In this particular experiment, a slight forcing at the natural wavelength has been applied to make the zigzag pattern perfectly periodic.

fluorescein marking the vortex pair. Views from above are also displayed in figure 11. The initial propagating velocity is $U_0 = 11.4\,\mathrm{mm\,s^{-1}}$ (closing time $T = 3.5\,\mathrm{s}$) so that the initial Froude number is $F_{h0} = 0.19$ while the initial Reynolds number is $Re_0 = 365$.

For the purpose of clearly demonstrating the development of the zigzag instability, a slight forcing has been applied at the natural wavelength of 6 cm by small adhesive tapes, 400 μm thick, 2.5 cm large, periodically placed on the inner side of each flap, out of phase between the two flaps. Indeed, when no forcing is applied, a large variability from one experiment to the other is observed as previously illustrated in figure 8 for two different experiments under identical conditions. Some experiments lead to a regular zigzag pattern (figure 8*a*) even though no forcing has been applied whereas, in others, defects or irregularly spaced deformations are observed (figure 8*b*). These irregularities can develop from background noise such as the residual motions that remain in the tank from a previous experiment despite having a 30 min minimum waiting time between experiments. Such sensitivity to external perturbations indicates that the selectivity of the instability is weak with a large bandwidth of unstable wavelengths. Confinement effects due to the finite height of the vortex pair can also be responsible for the presence of defects, although the ratio between the mean wavelength and the vortex pair length is about $\frac{1}{10}$. In contrast, a highly regular wavelength is always achieved when the instability is slightly forced, as seen in figure 10.

Shortly after the end of the flap motion, at $t = 7\,\mathrm{s}$ (figure 10*a*, *b*), the columnar vortex pair is initially straight and uniform along the vertical. At $t = 36\,\mathrm{s}$, it exhibits sinusoidal antisymmetric deformations which are best seen in the frontal view (figure 10*c*). Obviously, this antisymmetric instability differs from the Crow instability which is symmetric and ultimately produces vortex rings. Although it has the same symmetry as the elliptic instability, some differences are readily noticeable. As seen in figure 10(*c*), the whole vortex pair is bent without noticeable internal deformations. This contrasts with the elliptic instability (figure 7*a* and § 4.1) for which the mean axes of the two vortices remain globally straight, but the two vortex cores and envelopes are bent out of phase. When viewed from above at later time $t = 50\,\mathrm{s}$ (figure 11*b*), the vortex pair seems to be split into two distinct dipoles moving obliquely and symmetrically relative to the initial travelling direction.

By $t = 75\,\mathrm{s}$, in the frontal view (figure 10*e*), the amplitude of the deformations has increased dramatically. Nonetheless, the instability grows gently without any gravitational collapse and without subsequent large three-dimensional motions as it would for the elliptic instability (figure 7*b*). This distinct behaviour, i.e. the occurrence or not of the collapse phenomenon, has allowed us to unambiguously define a critical Froude number demarcating the elliptic and zigzag instabilities. Viewed from above (figure 11*c*), two groups of dipoles, propagating obliquely relative to the initial direction, are now clearly visible and well separated. Since the flow over the entire depth is visualized, these two dipoles correspond, in fact, to the extrema of the zigzag deformations half a wavelength apart in the vertical. These extrema are almost aligned along the vertical and appear superposed when viewed from above so that only two fuzzy dipoles are visible.

At $t = 121\,\mathrm{s}$ and $t = 176\,\mathrm{s}$ (figure 11*d*, *e*), the propagation directions of the two groups of dipoles keep turning and at the time of figure 11(*d*) they are propagating almost in opposite directions. When viewed from the side (figure 10*h*, *j*), the vortex pair exhibits a complex three-dimensional structure. At every wavelength, a dipole is propagating toward the viewer, while, behind, partly hidden by those in the front, the dipoles at every other half wavelength move away from the viewer. In the frontal view (figure 10*g*, *i*), the zigzag deformations grow further without any saturation although

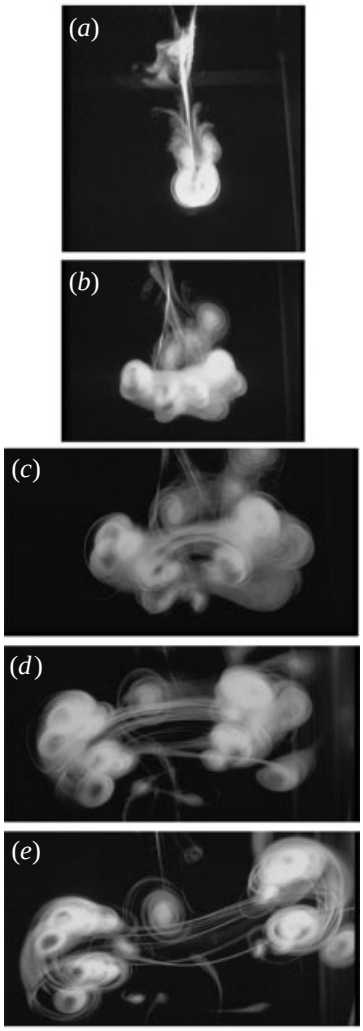

FIGURE 11. Views from above of the development of the zigzag instability for $F_{h0} = 0.19$ and $Re_0 = 365$. The pictures have been taken at approximately 20 s (*a*), 50 s (*b*), 75 s (*c*), 100 s (*d*), 180 s (*e*). These photographs are blurred because the flow over the entire depth is visualized. The trajectories of two group of dipoles located every half wavelength apart in the vertical are nonetheless clearly visible. This experiment is forced as in figure 10.

the vortices slow down by viscous diffusion. The columnar vortex pair is literally chopped into small individual pancake dipoles. This produces extreme vertical shear between vertically neighbouring 'pancake' dipoles which move away from each other. The dye connecting the vortices together are elongated into filaments (figure 10*g*, *j*). In figure 10(*g*), another phenomenon begins to be apparent: concurrently to the splitting of the columnar vortex pair into thin layers, a vertical realignment of the vortex core occurs inside each layer (figure 10*g*). Close-up views of this vertical realignment phenomenon are shown in figure 12. Such a process is not diffusive since the dye tracer is advected and does not seem to involve significant three-dimensional turbulent motions. This is testified by the fact that the core of the left vortex remains always well-defined.

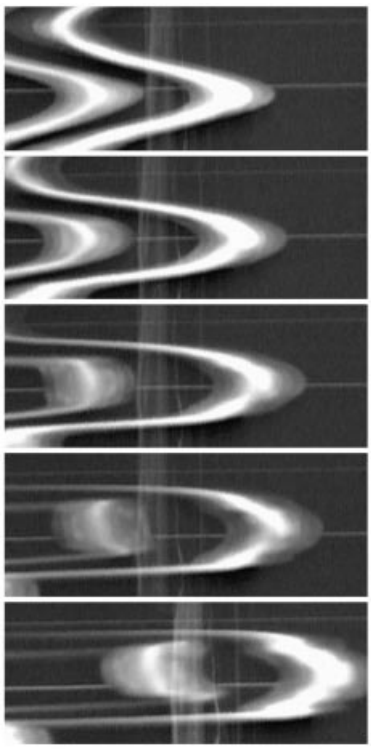

FIGURE 12. Close-up frontal view of the vertical realignment process. There is a 20 s time interval between each figure. $F_{h0} = 0.19$, $Re_0 = 365$.

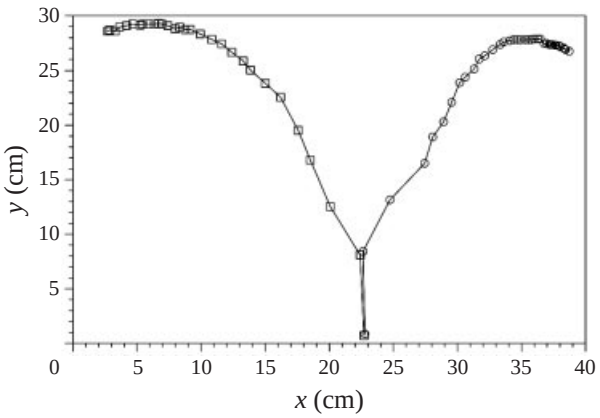

FIGURE 13. Trajectories of the centre of the two dipoles viewed from above. Each point is separated by a 15 s time interval. $F_{h0} = 0.19$ and $Re_0 = 365$.

The progressive rotation of the two set of dipoles and their propagation away from each other are further revealed in figure 13 where their whole trajectories seen from above are reported. At late times, they begin to go back toward the flaps but at this stage, the dipoles are close to the tank walls and may interact with them.

A three-dimensional sketch of the trajectories of each portion of the columnar vortex pair is displayed in figure 14. One of the most striking characteristics of this

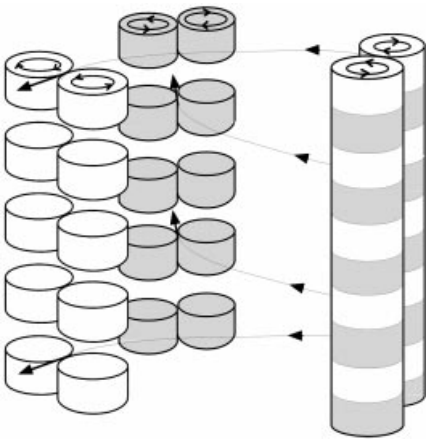

FIGURE 14. Three-dimensional sketch of the dipole trajectories viewed from the side as in figure 10.

instability is that the dipole structure in any horizontal cross-section is not appreciably modified. At a given vertical level, the dipole appears only to be rotated like a solid body. This vertically modulated twist modifies the propagating direction and results in a sinusoidal bend of the columnar vortex pair in the plane perpendicular to the travelling direction. The basic motions characterizing the instability are therefore a vertically modulated rotation associated to a translation perpendicular to the initial travelling direction.

It is relevant to wonder if this evolution might result from slow internal gravity waves that could induce horizontal motions varying along the vertical or to pre-existing vertically sheared mean horizontal flow as assumed by Majda & Grote (1998). To check that, vertical dye lines have been made by dropping fluorescent dye pellets at different distances from the vortex pair and at various times. These lines are not distorted and remain straight and vertical indicating that no vertically sheared mean horizontal flow is present and no noticeable internal gravity waves are radiated far from the vortex pair before or during the instability growth. This feature has also been confirmed by shadowgraph visualizations of the vortex pair.

4.4. *Late pancake structure*

Figures 15(*a*) and 15(*b*) display frontal and oblique close-up views of some pancake dipoles at time $t \approx 340$ s. As seen in figure 15(*b*), the flow in each layer has a very well-defined dipole form. The axis of the vortices through each layer is perfectly vertical (figure 15*a*). The filaments of dye connecting the vortices together are now only remnants and no longer mark active motions. In figure 15(*b*), we see that these dead filaments of dye are entrained and rolled up around each vortex of the pancake dipoles.

In contrast, we emphasize that the dipoles marked by fluorescein are still active. This feature can be shown easily by dropping fluorescent dye pellets close to the centre of one vortex of a pancake dipole as illustrated in the time sequence of figure 16. At $t = 220$ s (40 s after the drop), the dye line, that was initially straight, has spiralled once around the vortex centre (figure 16*a*). The spiral has a second turn at $t = 390$ s (figure 16*b*) and then a third turn by $t = 1050$ s (figure 16*c*). As guessed from figures 15(*a*) and 15(*b*), such spiralling motion indicates that the motion is confined to a layer, the horizontal velocity being highest in the middle horizontal plane of the vortex and decreasing away from this plane. The vertical shear implied by such a layered motion

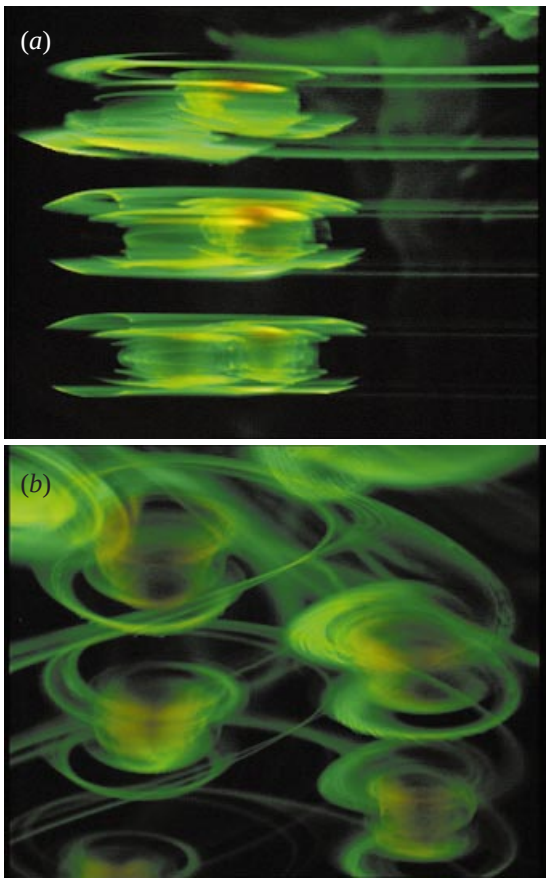

FIGURE 15. Close-up views of the 'pancake' dipoles filmed from (*a*) the front and (*b*) the side. The pictures have been taken at 336 s (*a*) and 348 s (*b*) after stopping the flap motion. Same experiment as in figure 10.

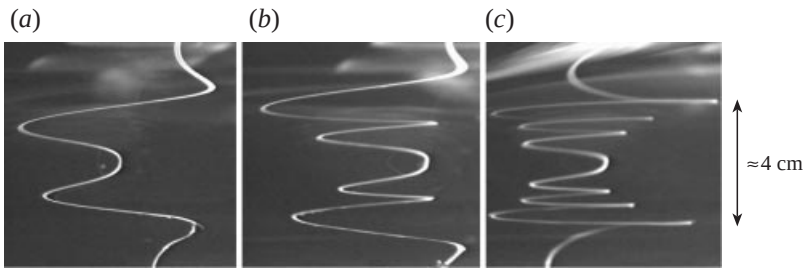

FIGURE 16. Visualizations of the deformation of a vertical dye line in a vortex of a pancake dipole. The dye line has been created at $t = 180$ s after the end of the flap motion. The pictures have been taken at (*a*) $t = 220$ s, (*b*) $t = 390$ s and (*c*) $t = 1050$ s. The fluid is still slowly moving at this time.

does not lead, however, to instability since no overturning motions are noticeable. At the top and bottom, the dye line has been entrained between figures 16(*b*) and 16(*c*) indicating that the vortex has diffused vertically.

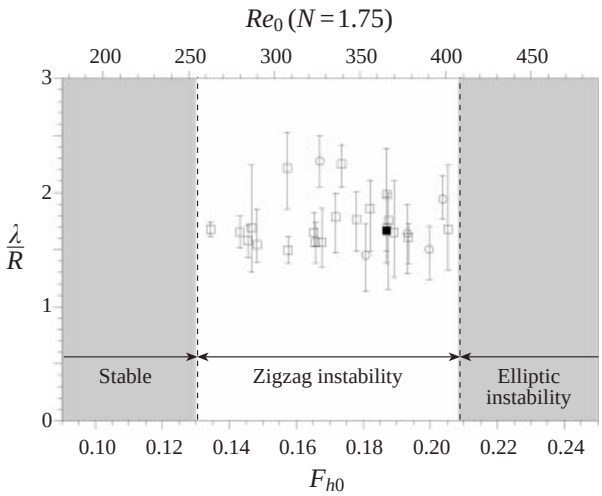

FIGURE 17. Non-dimensional wavelength λ/R as a function of the initial Froude number. □, $N = 1.75\,\mathrm{rad\,s^{-1}}$; ○, $N = 1.70\,\mathrm{rad\,s^{-1}}$; ■, forced experiment, $N = 1.75\,\mathrm{rad\,s^{-1}}$. The non-shaded domain is the region where the zigzag instability is observed alone.

4.5. *Wavelength measurements*

As mentioned in § 2, the natural wavelength of the instability has been measured from the frontal views in the unforced experiments. Figure 17 shows the measured wavelength non-dimensionalized by the dipole radius R as a function of the initial Froude number. These measurements have been carried out only when the zigzag instability is observed alone. Beyond the upper Froude number limit $F_{h0} > 0.21$, the elliptic instability develops prior to the zigzag instability as explained in § 4.1. On the low Froude number side, $F_{h0} < 0.13$, the vortex pair is stable and remains vertically uniform. Each point in figure 17 corresponds to a single unforced experiment for which the wavelength has been measured at two different times and averaged over 3 to 5 deformations typically observed in one experiment. The deformations near the bottom and the top of the tank have been excluded because of possible end effects. The error bars indicate the minimum and maximum wavelengths participating in the mean. There is a large dispersion both within one experiment and between two different experiments for the same parameter values. These fluctuations reflect the weak selectivity of the instability already mentioned in the previous section. The wavelength of the zigzag instability is about $\lambda \approx 1.7R$ but fluctuates between $1.1R$ and $2.5R$. Any conclusion on whether or not the wavelength depends on the Froude number cannot be safely given in regard of the narrowness of the instability range, $0.13 < F_{h0} < 0.21$, and the wavelength variability.

4.6. *Growth rate measurements*

The growth rates have been obtained from frontal views by measuring the amplitude of a single deformation of one vortex of the pair every 2 s over approximately 35 s. This measurement is started as soon as zigzags begin to be visible, i.e. between $t_b = 35$–50 s after the beginning of the flap motion. The amplitude is then corrected for the change in scale owing to the displacement of the dipole toward the camera. As shown in figure 18, the initial amplitude growth is well fitted by an exponential. Later, the amplitude grows linearly with time. This regime reflects the subsequent oblique quasi-steady propagation of the dipoles. For each experiment, the growth rate

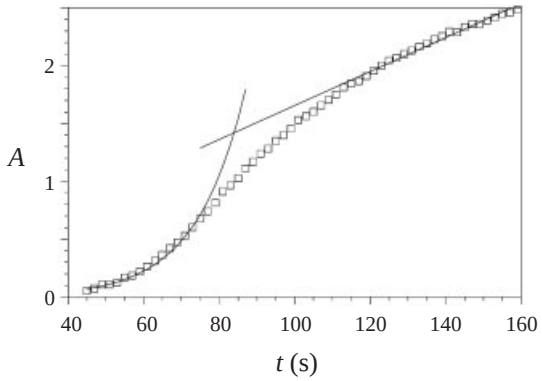

FIGURE 18. Example of determination of the growth rate for $F_{h0} = 0.18$, $Re_0 = 356$. The unit of the amplitude A is arbitrary.

has been extracted on two different zigzag deformations and averaged. The mean growth rate is displayed on figure 19(*a*) as a function of the initial Froude number (lower axis) or, equivalently, the initial Reynolds number (upper axis). The maximum growth rate occurs for $F_{h0} \approx 0.18$. The growth rate decreases approximately linearly to zero as the Froude number decreases to $F_{h0} = 0.13$.

The filled square represents the growth rate of the forced experiment. The effect of the forcing is to promote the instability development earlier, i.e. $t_b = 17$ s, than in the unforced experiments. The growth rate of this experiment is seen to be higher than in the unforced experiments (figure 19*a*) because the basic state has had less time to decay by viscous diffusion before the appearance of the instability. To take into account viscous damping, the velocity $U(t_b) = U_0 \exp(-t_b/\tau)$ measured at time t_b at which the instability begins to be visible is therefore more appropriate to scale the growth rate. This modified non-dimensional growth rate $\sigma R/U(t_b)$ is shown in figure 19(*b*) as a function of the effective Froude number at time t_b, $F_h = U(t_b)/NR$. In this plot, the points are shifted to higher growth rates and lower Froude numbers than in figure 19(*a*). Except for the forced case, the Froude number is reduced by approximately a factor of two while the growth rate increases by the same factor. The low Froude number threshold is now $F_h \approx 0.05$. This way of scaling the growth rate will allow a comparison with the numerical stability analysis (Billant & Chomaz 2000*b*) in which only the perturbation diffuses and not the basic state. In contrast, the wavelength has not been represented as a function of the effective Froude number F_h because the wavelength selection is expected to occur in the first stage of the instability development, i.e. well before the zigzags begin to be visible.

5. Conclusions

The 60 cm long columnar vertical vortex pair investigated in the present study has been generated with a flap apparatus. The basic vortex pair closely resembles the Lamb–Chaplygin dipole. When the fluid is strongly stratified, Crow and elliptic instabilities, usually observed in homogeneous fluid, are inhibited, but a new type of instability, called zigzag instability, has been identified. This instability is antisymmetric and consists of a vertically modulated twisting and bending of the vortex pair as a whole. The twist implies that the vortex pair propagates obliquely relative to the initial direction and in alternating directions every half wavelength. Kinematically, this twist accentuates the bending of the vortex pair perpendicularly to the dipole's

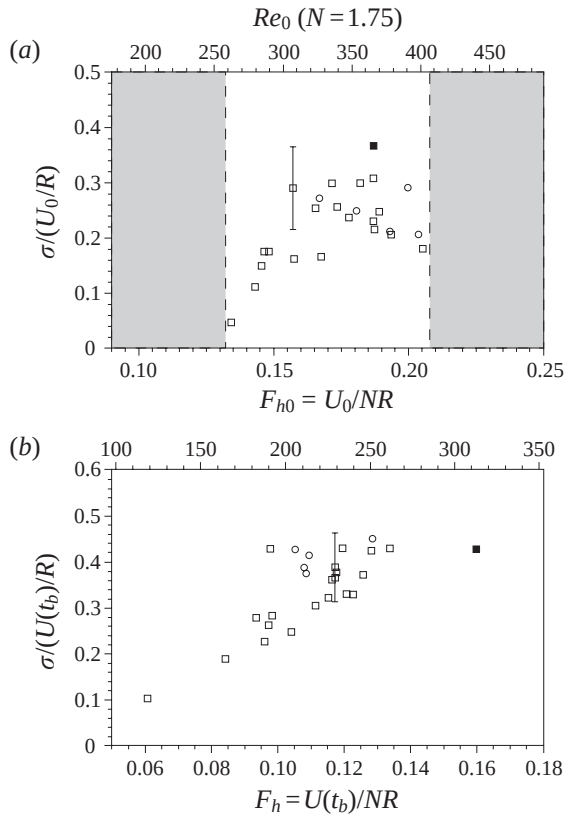

FIGURE 19. (*a*) Non-dimensional growth rate $\sigma R/U_0$ as a function of the initial Froude number F_{h0}. (*b*) Non-dimensional growth rate $\sigma R/U(t_b)$ as a function of the Froude number $F_h = U(t_b)/NR$. The approximate experimental error bar is shown on one point. □, $N = 1.75\,\mathrm{rad\,s^{-1}}$; ○, $N = 1.70\,\mathrm{rad\,s^{-1}}$; ■, forced experiment, $N = 1.75\,\mathrm{rad\,s^{-1}}$. In (*a*), the non-shaded domain is the region where the zigzag instability is observed alone.

initial travelling direction. The growth of the zigzags does not saturate and finally layers of individual pancake dipoles are produced. This process is accompanied by a vertical realignment of the vortex cores inside each layer. Such instability clearly differs from the symmetric Crow and antisymmetric elliptic instabilities. In the latter instability, the horizontal cross-sectional internal structure of the dipole is deformed whereas in the zigzag instability the dipole is rotated and translated like a solid body.

For buoyancy frequencies $N \leqslant 1.26\,\mathrm{rad\,s^{-1}}$, irregular zigzags are observed only after the development of the elliptic instability. For the largest Brunt–Väisälä frequency $N = 1.75\,\mathrm{rad\,s^{-1}}$ attainable in the present experimental conditions, the zigzag instability has been observed without the elliptic instability in the range $0.13 < F_{h0} < 0.21$. For $F_{h0} > 0.21$, the elliptic instability develops resulting in three-dimensional motions which subsequently collapse. Irregular zigzags then grow on the collapsed vortex pair. The threshold $F_{hc} = 0.2 \pm 0.01$ at which the elliptic instability is suppressed, is independent of the Brunt–Väisälä frequencies investigated ($1.26 \leqslant N \leqslant 1.97$) and in good agreement with the value $F_{hc} = 0.22$ obtained from the theoretical study of Miyazaki & Fukumoto (1992).

Below $F_{h0} < 0.13$, the vortex pair is stable, probably because of viscous effects since the associated Reynolds number, $Re_0 < 260$, is low. This stabilization occurs despite

the fact that we have increased the Brunt–Väisälä frequency to its maximum value in order to achieve the maximum Reynolds number for a given Froude number. This viscous 'doom' of the low Froude number regime is not specific to the present study but to all laboratory experiments because the size of experimental apparatus and the buoyancy frequency achievable are limited. In contrast, geophysical flows, owing to their large size, are characterized by large Reynolds number and low Froude number. For such flows, we expect that the low Froude number cutoff will be lower. In order to explore the nearly inviscid low Froude number regime pertaining to geophysical flows, we have carried out two companion studies (Billant & Chomaz 2000*a*, *b*). In Billant & Chomaz (2000*a*), we have performed an inviscid asymptotic stability analysis of a columnar vortex pair for small Froude number and long-wavelength. Besides explaining its physical mechanism, this study predicts that the zigzag instability exists for arbitrary small Froude number with a wavelength scaling as U/N in the inviscid limit. Therefore, as expected, the low Froude number cutoff is controlled by viscous effects and tends to zero in the inviscid limit. Yet, in the present experiments, the measured wavelength is roughly constant $\lambda \approx 1.7R$ over the range $0.13 < F_{h0} < 0.21$. It should be borne in mind, however, that this absence of variation is likely to result from the narrowness of the unstable Froude number range with respect to the high natural variability of the instability wavelength. To further resolve this apparent contradiction, a numerical stability analysis, in which the Froude and Reynolds numbers are varied over a wide range, is conducted in Billant & Chomaz (2000*b*). On one hand, the numerical results for large Reynolds numbers confirm the theoretical inviscid scaling law. On the other hand, the numerical results for low Reynolds number agree with the present experimental measurements of growth rate and wavelength. Furthermore, the zigzag instability is damped below a critical Froude number as in the experiments. Billant & Chomaz (2000*b*) thus ties together both the present experimental study and the theoretical analysis giving a consistent picture of the zigzag instability.

We conjecture that the observed multiple-layer phenomena in numerical, laboratory and field experiments might have such an instability as a generation mechanism. However, we stress that a low horizontal Froude number and a high Reynolds number are required together with the presence of several interacting vertical vortices that are sufficiently tall relative to the instability wavelength. In this respect, it may be noted that the decoupling behaviour of the zigzag instability resembles those of the three-dimensional instabilities reported by Dritschel & Torre Juárez (1996) in numerical simulations of multi-columnar vortices in a rapidly rotating and strongly stratified fluid (quasi-geostrophic flow). This suggests that decoupling instabilities might persist in the presence of a background rotation even if the Coriolis force is expected to increase the vertical coherence. A parametric study of a strongly stratified flow in which an additional background rotation is varied over a wide range would, however, be necessary to determine whether the three-dimensional instabilities observed in quasi-geostrophic and strongly stratified flows have the same physical origin.

We thank warmly A. Garcia and J. Webert for technical assistance and C. H. K. Williamson and T. Leweke for providing the flap apparatus. We are indebted to the audio-visual team of the École Polytechnique, J. F. Beraud, P. Gaucherand, P. Lavialle and C. Witz, for the photography. Precise measurements were made possible by the CIV software provided by A. Fincham and G. Spedding. The authors wish to thank O. Eiff for his careful reading of the manuscript.

REFERENCES

Batchelor, G. K. 1967 *An Introduction to Fluid Dynamics*. Cambridge University Press.

Billant, P. & Chomaz, J.-M. 2000*a* Theoretical analysis of the zigzag instability of a vertical columnar vortex pair in a strongly stratified fluid. *J. Fluid Mech.* **419**, 29–63.

Billant, P. & Chomaz, J.-M. 2000*b* Three-dimensional stability of a vertical columnar vortex pair in a stratified fluid. *J. Fluid Mech.* **419**, 65–91.

Bonnier, M., Eiff, O. & Bonneton, P. 2000 On the density structure of far wake vortices in a stratified fluid. *Dyn. Atmos. Oceans* **31**, 117–137.

Chomaz, J. M., Bonneton, P., Butet, A. & Hopfinger, E. J. 1993 Vertical diffusion in the far wake of a sphere moving in a stratified fluid. *Phys. Fluids* A **5**, 2799–2806.

Crow, S. C. 1970 Stability theory for a pair of trailing vortices. *AIAA J.* **8**, 2172–2178.

Dritschel, D. G. & Torre Juárez, M. de la 1996 The instability and breakdown of tall columnar vortices in a quasi-geostrophic fluid. *J. Fluid Mech.* **328**, 129–160.

Fincham, A. M., Maxworthy, T. & Spedding, G. R. 1996 Energy dissipation and vortex structure in freely decaying stratified grid turbulence. *Dyn. Atmos. Oceans* **23**, 171–182.

Fincham, A. M. & Spedding, G. R. 1997 Low cost, high resolution DPIV for measurement of turbulent fluid flow. *Exps Fluids* **23**, 449–462.

Flor, J. B. & Van Heijst, G. J. F. 1994 An experimental study of dipolar vortex structures in a stratified fluid. *J. Fluid Mech.* **279**, 101–133.

Gregg, M. C. 1987 Diapycnal mixing in the thermocline: a review. *J. Geophys. Res.* **92**, 5249–5286.

Herring, J. R. & Métais, O. 1989 Numerical simulations in forced stably stratified turbulence. *J. Fluid Mech.* **202**, 97–115.

Hopfinger, E. J. 1987 Turbulence in stratified fluids: a review. *J. Geophys. Res.* **92**, 5287–5303.

Kimura, Y. & Herring, J. R. 1996 Diffusion in stably stratified turbulence. *J. Fluid Mech.* **328**, 253–269.

Leweke, T. & Williamson, C. H. K. 1998 Cooperative elliptic instability of a vortex pair. *J. Fluid Mech.* **360**, 85–119.

Lin, J. T. & Pao, Y. H. 1979 Wakes in stratified fluids: a review. *Ann. Rev. Fluid Mech.* **11**, 317–338.

Majda, A. J. & Grote, M. J. 1998 Model dynamics and vertical collapse in decaying strongly stratified flows. *Phys. Fluids* **9**, 2932–2940.

Meleshko, V. V. & Heijst, G. J. F. van 1994 On Chaplygin's investigations of two-dimensional vortex structures in an inviscid fluid. *J. Fluid Mech.* **272**, 157–182.

Métais, O., Bartello, P., Garnier, E., Riley, J. J. & Lesieur, M. 1996 Inverse cascade in stably stratified rotating turbulence. *Dyn. Atmos. Oceans* **23**, 193–203.

Métais, O. & Herring, J. R. 1989 Numerical simulations of freely evolving turbulence in stably stratified fluids. *J. Fluid Mech.* **202**, 117–148.

Miyazaki, T. & Fukumoto, Y. 1992 Three-dimensional instability of strained vortices in a stably stratified fluid. *Phys. Fluids* A **4**, 2515–2522.

Nguyen Duc, J. M. & Sommeria, J. 1988 Experimental characterization of steady two-dimensional vortex couples. *J. Fluid Mech.* **192**, 175–192.

Riley, J. J., Metcalfe, R. W. & Weissman, M. A. 1981 Direct numerical simulations of homogeneous turbulence in density stratified fluids. In *Proc. AIP Conf. Nonlinear Properties of Internal Waves* (ed. B. J. West), 79–112.

Spedding, G. R 1997 The evolution of initially turbulent bluff-body wakes at high internal Froude number. *J. Fluid Mech.* **337**, 283–301.

Spedding, G. R., Browand, F. K. & Fincham, A. M. 1996 Turbulence, similarity scaling and vortex geometry in the wake of a sphere in a stably-stratified fluid. *J. Fluid Mech.* **314**, 53–103.

Thomas, P. J. & Auerbach, D. 1994 The observation of the simultaneous development of a long- and a short-wave instability mode on a vortex pair. *J. Fluid Mech.* **265**, 289–302.

Tsai, C. Y. & Widnall, S. E. 1976 The stability of short waves on a straight vortex filament in a weak externally imposed strain field. *J. Fluid Mech.* **73**, 721–733.

Waleffe, F. 1990 On the three-dimensional instability of strained vortices. *Phys. Fluids* A **2**, 76–80.

Williamson, C. H. K. & Chomaz, J. M. 1997 The exploding vortex pair. *Phys. Fluids* **9**, 54.